Journal of Computational Physics **173,** 61–86 (2001)
doi:10.1006/jcph.2001.6842, available online at http://www.idealibrary.com on IDEAL®

Large-Scale Simulations of Microstructural Evolution in Elastically Stressed Solids

Norio Akaiwa,* K. Thornton,†,‡ and P. W. Voorhees†

*National Research Institute for Metals, Tsukuba, Japan; †Department of Materials Science and Engineering, Northwestern University, Evanston, Illinois 60208; ‡Department of Materials Science and Engineering, Massachusetts Institute of Technology, Cambridge, Massachusetts 02139
E-mail: k-thornton@northwestern.edu

Received June 4, 2000; revised May 24, 2001

We present a set of numerical methods for simulations of microstructural evolution in elastically stressed solids. We combine three powerful tools to achieve computational efficiency: the boundary integral method to provide excellent resolution, the fast multipole method to reduce computational cost, and the small-scale decomposition technique with a two-level time-stepping scheme to remove the stiffness from the time advance. Although we apply these methods to study the topic of our interest, the details of how they are implemented can be useful in many other situations. We extend the fast multipole method to calculate the anisotropic stress field in periodic two-dimensional domains and in doing so address issues associated with the conditional convergence of the summations. In addition, we introduce a new formula for the potential in periodically arranged two-dimensional cells in the absence of an applied field through a summation in physical space without using the Ewald sum. Furthermore, we implement a time-stepping scheme that enables us to speed up the calculation by an additional factor of 100 over a straightforward implementation of the small-scale decomposition technique. The computational complexity scales as the number of mesh points N, and thus we are able to employ $N \sim 500,000$ in a typical calculation.

Key Words: fast multipole method; boundary integral method; Ostwald ripening; periodic potential; anisotropic elasticity.

1. INTRODUCTION

Microstructures consisting of matrix and particle phases in metals are of industrial interest since the sizes and shapes of the particles can control the physical characteristics of the material. In such materials, thermomechanical processing is employed to achieve the desired properties. These processes typically involve aging at elevated temperatures where

0021-9991/01 $35.00

solid-state diffusion is significant. Under these conditions, the second-phase particles can grow and their average size increases via a process known as Ostwald ripening, or coarsening. The coarsening process is well understood theoretically when the only driving force for the coarsening process is the surface energy. In this case, the system evolves to reduce the total interfacial energy, which is linearly proportional to the interfacial area. Therefore, the evolution proceeds by larger particles growing at the expense of smaller particles. Lifshitz and Slyozov [19] and Wagner [36] (LSW) described this process in the limit of a zero volume fraction of particle phase and found a self-similar growth characterized by a single length scale, $R(t)$, where R is the average particle size, that varies as $\sim t^{1/3}$. Systems with nonzero volume fractions have also been studied; see [1, 20, 21] and references therein. These theories find that the temporal power laws for the average particle size predicted by LSW remain unchanged by a nonzero volume fraction; however, the amplitudes of the temporal power laws were found to depend on the volume fraction of coarsening phase. Specifically, the constant K in $R^3(t) \sim Kt$ is predicted to increase monotonically with the volume fraction.

In two-phase solid systems, the difference in the lattice parameters of the matrix and particle phases, or the misfit, gives rise to a long-range elastic field. This contributes additional energy to the system. It is not known quantitatively how elastic stress modifies the statistically averaged properties of the Ostwald ripening process, but much qualitative information indicates that the changes are significant. The effects of elastic stress on the evolution of the microstructure have been studied extensively in model alloys such as Ni-Al, where there is a misfit between the particles and the matrix. Experimental results clearly show changes in the microstructure as elastic energy becomes important (see, for example, [4]). They show microstructures consisting of particles with various shapes and symmetries that depend on the magnitude and symmetry of the elastic stress. For example, in cubic alloys with a dilatational misfit, such as the Ni-Al system studied by Ardell and Nicholson, the particle shape changes from a sphere to a cuboid as the relative importance of the elastic energy (proportional to the volume) to the interfacial energy (proportional to the interfacial area) increases along with the average particle size [4]. At still larger sizes, the cuboids change to plate-like or rod-like shaped particles. Furthermore, at the same time the particles align themselves along the elastically soft $\langle 100 \rangle$ directions of the crystal. This change in the microstructure modifies the properties of the material, and finding a practical method to control it is an important issue in the metallurgical community.

The evolution of microstructure in elastically stressed solids has been well studied via a number of numerical techniques. Computational simulations of particle coarsening in elastically stressed solids have been performed using diffuse interface models [17, 24, 29, 37], Ising models [9, 16], and sharp interface models [14, 35]. They show that the particle shape evolution from spheres to cuboids, and then to plates, is the direct result of the anisotropic elastic energy. The results are qualitatively consistent with experimental results. In addition, the calculated spatial distribution of the particles is similar to those observed in experiments. However, these simulations were performed using relatively small system sizes (order of 10 particles in many cases), and they do not provide enough information to characterize the microstructure quantitatively, or to determine the evolution of the statistically averaged properties of these ensembles. The challenge of extending these calculations to systems with many thousands of particles is that the shapes of the particles cannot be constrained, but must evolve in a manner that is consistent with the diffusion and stress fields in the system. Thus, one must solve a multibody free-boundary problem involving diffusion

and stress fields that evolve with the microstructure. Although phase field methods have advantages, such as the ability to accommodate particle coalescence and disappearance, they have difficulties matching the excellent resolution of the interfaces that sharp-interface models provide in systems with large number of particles. Given the goal of simulating systems containing large number of particles, we choose the sharp interface formulation of the problem.

In this paper, we describe the method which enables us to perform large-scale simulations of elastically stressed solids accurately and efficiently. It is made possible through a combination of advanced numerical methods—the boundary integral method, the fast multipole algorithm, and a two-level time-stepping technique along with the small-scale decomposition, or the θ-L formulation—modified to work together in our specific case. We outline the method to combine these formulations and give detailed descriptions of modifications that were made. The methods that we have implemented will be useful for other problems as well.

2. THEORETICAL BACKGROUND

Consider a two-phase solid system wherein the particles and the matrix possess different lattice parameters, the interfaces between the particles and the matrix are coherent, and the Ostwald ripening process occurs via the diffusion of mass. Following [34], we nondimensionalize the dimensional concentration field, C, by

$$u = \frac{(C - C_\infty^\alpha)l}{l_c C_\infty^\alpha}, \tag{1}$$

and the dimensional time, T, by

$$t = T/\tilde{t}, \tag{2}$$

where

$$\tilde{t} = \frac{\zeta l^2}{D}, \tag{3}$$

$$\zeta = \frac{(C_\infty^\beta - C_\infty^\alpha)l}{l_c C_\infty^\alpha}, \tag{4}$$

C_∞ is the value of C at a flat interface, superscripts α and β denote the matrix and particle phases, respectively, l is the length scale used in nondimensionalization, l_c is the capillary length, and D is the diffusion coefficient. The length scale l may be taken to be the particle size, or, if many particles are present, either the size of the computational domain in dimensional units or the initial average particle size. All variables in this paper are nondimensionalized unless otherwise noted. Assuming that the motion of the interfaces is slow compared to the relaxation time for the concentration field, a good assumption during coarsening, u in the matrix phase satisfies the steady-state diffusion equation,

$$\nabla^2 u(\mathbf{x}) = 0. \tag{5}$$

We assume periodic boundary conditions for the computational domain for our calculations. The concentration at the particle–matrix interface is given by the stress-modified Gibbs–Thomson equation [12],

$$u(\mathbf{x}) = \kappa + L\left\{\frac{1}{2}[\![\mathbf{T}\cdot\tilde{\mathbf{E}}]\!] - \mathbf{T}^{\alpha}\cdot[\![\mathbf{E}]\!]\right\}, \tag{6}$$

where κ is the curvature, $\mathbf{T}$ is the dimensionless elastic stress, $\tilde{\mathbf{E}}$ is the scaled elastic strain, $\mathbf{E}$ is the scaled total strain, and $[\![f]\!] = f^{\beta} - f^{\alpha}$ for a quantity f at the interface. L is a dimensionless parameter [28] which is defined as

$$L = \frac{\epsilon^2 C_{44} r}{\sigma}, \tag{7}$$

where ϵ is the magnitude of the dilatational misfit, C_{44} is one of the dimensional elastic constants in this cubic alloy, r is the dimensional effective radius of the particle, and σ is the dimensional interfacial energy. By this definition, the dimensionless elastic constants are normalized to C_{44}, $\mathbf{T} = \mathbf{t}/(C_{44}\epsilon)$, $\mathbf{E} = \mathbf{e}/\epsilon$, and $\tilde{\mathbf{E}} = \tilde{\mathbf{e}}/\epsilon$, where $\mathbf{t}$, $\mathbf{e}$, and $\tilde{\mathbf{e}}$ are the corresponding dimensional quantities. Here, the effective radius of a noncircular particle is defined as $r = \sqrt{A/\pi}$, where A is the area of the (two-dimensional) particle, and we have assumed that the lattice parameter of the phases and elastic constants are not functions of composition.

The parameter L gives the relative importance of the elastic energy compared to the interfacial energy. In each simulation, we assign the ratio $\epsilon^2 C_{44}/\sigma$ to the system. This gives the value of L for each particle. Since L is proportional to the radius of the particle, $\langle L\rangle$ increases as time increases. Therefore, the stress effects become more important as coarsening proceeds.

The evolution of the interface is given by the interfacial mass balance,

$$V(\mathbf{x}) = \frac{\partial u}{\partial n}, \tag{8}$$

where V is the normal velocity of the interface, $\mathbf{x}$ is a point on the interface, and n is the coordinate along the normal $\mathbf{n}$. We also constrain the total volume of particle phase to be constant,

$$\sum_{j=1}^{M}\int_{\gamma_j} V(\mathbf{x})\, ds_j = 0, \tag{9}$$

where ds_j is the arc length element of the interface γ_j of the j-th particle and M is the total number of particles. After solving Eq. (5) with the boundary condition Eq. (6), the interface is updated using the normal velocity given in Eq. (8). When a particle becomes very small ($r < 0.05\langle r\rangle$, equivalent to 0.25% in area compared to that of the average-sized particle), it is assumed to have disappeared and is removed from the calculation. The mass conservation constraint (Eq. (9)) implies that the area fraction of particle phase remains constant. We therefore make a very small adjustment to the area fraction of the particle phase to compensate for the removed particle area.

In mechanical equilibrium, the stress field satisfies

$$\sum_{j=1}^{3} T_{ij,j} = 0, \quad i = 1, 2, 3, \tag{10}$$

with the boundary conditions at the matrix–particle interfaces

$$\sum_{j=1}^{3} [\![T_{ij}]\!] n_j = 0, \quad i = 1, 2, 3, \tag{11}$$

$$[\![U_i]\!] = 0, \quad i = 1, 2, 3, \tag{12}$$

where U_i is the i-th component of the displacement vector, and the comma denotes differentiation in the direction indicated by the index. We take the system to be elastically homogeneous and anisotropic. This enables us to obtain the stress and strain fields at the interfaces through the Green's function corresponding to Eqs. (10)–(12) [23]. The stresses and strains that appear in Eq. (6) are then calculated by determining the scaled displacement gradient along the interface,

$$U_{j,k}(\mathbf{x}) = \sum_{n=1}^{M} \sum_{i,l,m=1}^{3} c_{ilmm} \int_{\gamma_n} g_{ij,k}(\mathbf{x}, \mathbf{x}') n_l' \, ds', \tag{13}$$

where c_{ijkl} is the dimensionless elastic constant tensor with cubic symmetry, g_{ij} is the dimensionless anisotropic elastic Green's function tensor, $\mathbf{x}$ and $\mathbf{x}'(s')$ are points on the interface, and s' is the arc length coordinate. The stress and strain are then determined using the derivatives of the displacement and the constitutive relations of anisotropic linear elasticity, namely,

$$T_{ij} = \sum_{k,l=1}^{3} c_{ijkl} \tilde{E}_{kl}, \tag{14}$$

$$E_{ij} = \frac{1}{2}(U_{i,j} + U_{j,i}), \tag{15}$$

and $\tilde{E}_{ij}^{\alpha}$ and $\tilde{E}_{ij}^{\beta}$ are given by

$$\tilde{E}_{ij}^{\alpha} = E_{ij}^{\alpha}, \tag{16}$$

$$\tilde{E}_{ij}^{\beta} = E_{ij}^{\beta} - \delta_{ij}, \tag{17}$$

where δ_{ij} is the Kronecker delta. Other crystal symmetries can be accommodated since the Stroh theory yields an essentially analytic Green's function in the same form considered in this paper. So far, we have only implemented an extension to a tetragonal misfit, and we have made some simulations with good results.

The set of equations, Eqs. (5)–(13), is to be solved for a system of particles with arbitrary shapes. Complications arise because of the nonlinear nature of the boundary condition Eq. (6), not only as a result of the curvature dependence in the Gibbs–Thomson equation, but also as a result of the elastic stress. (The field equations are linear.) We adopt the boundary integral technique to solve this free-boundary problem accurately and efficiently. Further details are given in Section 5.1.

3. ELASTIC FIELD

An efficient implementation of the quadrature shown in Eq. (13) requires knowledge of the Green's function. In two dimensions, a particularly advantageous representation of the Green's function can be obtained using Stroh theory [5],

$$g_{jk}(\mathbf{x}-\mathbf{x}') = -\frac{1}{2\pi i}\sum_{\alpha=1}^{6} \pm A_{j\alpha}A_{k\alpha}\ln(\mathbf{m}\cdot(\mathbf{x}-\mathbf{x}') + \lambda_\alpha \mathbf{n}\cdot(\mathbf{x}-\mathbf{x}')), \tag{18}$$

where $\mathbf{m} = (\cos\theta, \sin\theta, 0)$, $\mathbf{n} = (-\sin\theta, \cos\theta, 0)$, and θ is the angle between the x-axis and the vector $\mathbf{m}$. Note that $\mathbf{m}$ and $\mathbf{n}$ are orthogonal and α denotes different sets of eigenvalues and eigenvectors. $\mathbf{A}_\alpha$ and λ_α satisfy the following equation,

$$\sum_{i,k,m=1}^{3} c_{ijkm}(m_i + \lambda_\alpha n_i)(m_m + \lambda_\alpha n_m)A_{k\alpha} = 0. \tag{19}$$

Equation (19) can be transformed to a six-dimensional eigenvalue problem by introducing the associated vector $\mathbf{L}_\alpha$ [5],

$$L_{j\alpha} = \sum_{i,k,m=1}^{3} -n_i c_{ijkm}(m_m + \lambda_\alpha n_m)A_{k\alpha}, \tag{20}$$

or equivalently,

$$L_{j\alpha} = \sum_{i,k,m=1}^{3} \frac{1}{\lambda_\alpha} m_i c_{ijkm}(m_m + \lambda_\alpha n_m)A_{k\alpha}, \tag{21}$$

with the normalization condition,

$$\sum_{j=1}^{3} A_{j\alpha}L_{j\alpha} = \frac{1}{2}. \tag{22}$$

Thus, $\mathbf{A}_\alpha$ and λ_α are the eigenvector and eigenvalue, respectively.

In our calculation, we need the eigenvalues, λ_α, $\alpha = 1, 2, \ldots, 6$, and the products of the eigenvectors components, $A_{1\alpha}^2$, $A_{2\alpha}^2$, and $A_{1\alpha}A_{2\alpha}$. For cubic symmetry, these can be found analytically for $\mathbf{m} = (1, 0, 0)$ and $\mathbf{n} = (0, 1, 0)$, resulting in six eigenvalues. For $\lambda_\alpha = \pm i$, all relevant products of $A_{j\alpha}$'s are identically zero, and therefore the associated terms do not contribute. For the rest of the eigenvalues,

$$\lambda_\alpha = f + g,\ f - g, -f + g, -f - g, \tag{23}$$

where

$$f = \sqrt{\frac{(C_{11}+C_{12})(2C_{44}-C_{11}+C_{12})}{4C_{11}C_{44}}}, \tag{24}$$

$$g = \sqrt{\frac{(-C_{11}+C_{12})(2C_{44}+C_{11}+C_{12})}{4C_{11}C_{44}}}. \tag{25}$$

C_{ij}'s are contracted (Voigt) elastic constants [23], and

$$A_{1\alpha}^2 = \frac{\lambda_\alpha\left(C_{44} + C_{11}\lambda_\alpha^2\right)}{2C_{11}C_{44}\left(1-\lambda_\alpha^4\right)}, \tag{26}$$

$$A_{2\alpha}^2 = \frac{\lambda_\alpha\left(C_{11} + C_{44}\lambda_\alpha^2\right)}{2C_{11}C_{44}\left(1-\lambda_\alpha^4\right)}, \tag{27}$$

$$A_{1\alpha}A_{2\alpha} = -\frac{\lambda_\alpha^2(C_{12}+C_{44})}{2C_{11}C_{44}\left(1-\lambda_\alpha^4\right)}. \tag{28}$$

The eigenvalues and the eigenvectors need to be computed only once at the beginning of the simulation for the specified elastic constants. Although there are four contributing eigenvalues, two sets of two terms give the same results. Therefore, the integral in Eq. (13) with the Green's function defined in Eq. (18) must be performed only twice, not four times. The elastic interaction is long ranged, and thus we cannot impose a cutoff distance for the interaction. Consequently, the Green's function in Eq. (18) needs to be integrated for all pairs of $\mathbf{x}$ and $\mathbf{x}'$. The direct summation would result in a complexity of $O(N^2)$, where N is the number of mesh points, making a large-scale simulation impossible. Therefore, a modified fast multipole method (FMM) is adopted to remove this obstacle.

4. THE POTENTIAL IN A PERIODICALLY ARRANGED CELL

Since the FMM sums in physical space, it is necessary to determine potentials in a system with periodically repeated cells. The potential resulting from long-range interactions between particles and their periodic images is often important. Typically, when potentials are calculated in physical space, the Ewald sum [3] has been applied. The method involves summation in both physical space and in reciprocal (Fourier) space, and there are a few parameters that need to be chosen depending on the specifics of the simulated systems. Schmidt and Lee derived a method to convert the FMM potential to one consistent with the Ewald sum by comparing the expressions resulting from each method [26]. They obtained a correction term for a three-dimensional problem in terms of multipole moments and spherical harmonics. In another work, the periodic contribution to a sum was calculated via FMM summation over the repeated (image) cells [8]. While the FMM is very efficient in calculating sums in a large domain, this approach requires more computational time than that required for a calculation over one cell. In another approach, fictitious charges are added to cancel the net dipole moment in the unit cell so that the correction term becomes zero, thus obviating the need to correct for the dipole-induced surface charge on the unit cell [15]. Although the potential resulting from this approach does give the correct derivative of the potential that takes into account the potentials generated by the image cells, the potential itself is shifted by an arbitrary constant. Therefore, this approach is not appropriate in some situations, such as energy calculations, where the absolute value of the result is important. In this section, we develop compact formulae for periodic potentials resulting from monopoles and dipoles in two-dimensional space. The new method is much more straightforward compared to the previous approaches and greatly improves the ability to work with numerical methods such as the FMM. The additional computational time to account for the interaction with periodic images is small as it is included in the analytic expression for the potential in terms of a multipole expansion. There are no parameters

to adjust to achieve certain accuracy because it is an exact formula (other than the usual truncation of multipole terms). We then employ these expressions to derive the potentials in periodically arranged cells for the elasticity, as well as for the diffusion problems.

We assume that the computational domain of unit size is repeated periodically to fill all two-dimensional space. In the absence of an applied field, the potential is periodic with a period of unity, because of the effects from all particles in the repeated cells. We must be able to calculate these effects without directly summing the actual potentials from each particle in the repeated cells. A multipole expansion can be used to carry this out, but a straightforward calculation results in a potential without proper periodicity. As we address later, this is due to the conditionally convergent term; that is, the numerical value of the term depends on how the sum is taken, and it requires special attention to reach the correct result for a particular application.

Consider a potential at $\mathbf{x}$ generated by charges q_j at locations $\mathbf{x}_j$,

$$\phi(\mathbf{x}) = \sum_{j=1}^{N} q_j \log|\mathbf{x}_j - \mathbf{x}|, \tag{29}$$

and by dipoles with strength p_j and direction $\mathbf{n}_\mathrm{j}$,

$$\psi(\mathbf{x}) = \sum_{j=1}^{N} p_j \frac{\partial}{\partial n_j} \log|\mathbf{x}_j - \mathbf{x}|, \tag{30}$$

where n_j is the coordinate along $\mathbf{n_j}$. Here, n_{jx} and n_{jy}, are the x- and y-components of $\mathbf{n_j}$, respectively, given by

$$n_{jx} = \frac{\partial x_j}{\partial n_j}, \tag{31}$$

$$n_{jy} = \frac{\partial y_j}{\partial n_j}. \tag{32}$$

Writing in complex form, the potentials can be expressed as

$$w_\phi(\mathrm{Z}) = \sum_{j=1}^{N} q_j \log(z_j - z), \tag{33}$$

and

$$\begin{aligned} w_\psi(\mathrm{Z}) &= \sum_{j=1}^{N} p_j \frac{\partial}{\partial n_j} \log(z_j - z) \\ &= \sum_{j=1}^{N} \frac{\mu_j}{z_j - z}, \end{aligned} \tag{34}$$

where $\mathbf{x} = (x, y)$ is expressed in terms of complex variable $z = x + iy$, and $\mu_j = p_j(n_{jx} + in_{jy})$ is the complex dipole charge. Note that the real part of $w_\phi(z)$ and $w_\psi(z)$ is identical to $\phi(\mathbf{x})$ and $\psi(\mathbf{x})$, respectively.

We first focus on the dipole potential, $w_\psi(z)$. Assume the sources are located in a unit cell which is repeated to fill the two-dimensional space completely. Let ζ_k be the location of the center of the k-th cell, and we apply the multipole expansion. Splitting the summation in three parts, a term corresponding to the central cell, a sum for the surrounding eight cells (nearby cells) and another for the rest (well-separated cells),

$$\begin{aligned} w_\psi(z) &= \sum_{j=1}^{N} \sum_{k} \frac{\mu_j}{z_j - z + \zeta_k} \\ &= \sum_{j=1}^{N} \mu_j \left(\frac{1}{z_j - z} + \sum_{k}{}' \frac{1}{z_j - z + \zeta_k} + \sum_{k}{}'' \frac{1}{z_j - z + \zeta_k} \right). \end{aligned} \tag{35}$$

Here, the summation over k for the nearby cells is denoted by $\sum'$ and the summation over the rest (well separated cells) by $\sum''$. The last term in the right-hand side of Eq. (35) is rewritten as a multipole expansion,

$$\begin{aligned} \sum_{j=1}^{N} \mu_j \sum_{k}{}'' \frac{1}{z_j - z + \zeta_k} &= \sum_{j=1}^{N} \mu_j \sum_{k}{}'' \sum_{m=0}^{\infty} \frac{1}{\zeta_k} \left(\frac{z - z_j}{\zeta_k} \right)^m \\ &= \sum_{j=1}^{N} \mu_j \sum_{m=0}^{\infty} \tilde{S}_{m+1} (z - z_j)^m, \end{aligned} \tag{36}$$

where $\tilde{S}_m$ is the (partial) lattice sum,

$$\tilde{S}_m = \sum_{k}{}'' \frac{1}{\zeta_k^m}. \tag{37}$$

This lattice sum excludes the part that is due to the nearby cells in the usual (complete) lattice sum, which is given by

$$S_m = \sum_{k} \frac{1}{\zeta_k^m}, \tag{38}$$

in which the sum goes over all cells other than the one at the origin. All S's but S_2 can be computed using the renormalization method [6]. For a square unit cell, S_m for $m = 4l$, where l is an integer, converges absolutely to nonzero real values, which have been tabulated in [6]. In addition, both S_m and $\tilde{S}_m$ are zero for all m except $m = 2$ and $m = 4l$ in this case. The value of $\tilde{S}_m$ depends on the shape of the unit cell since the part that is absent in $\tilde{S}_m$ is shape dependent. Computing the value of S_2 is not as straightforward as this is not absolutely convergent, and the value depends on how the sum is computed. For example [7, 11],

$$S_2 = \begin{cases} 0 & \text{circular or square shape of summation} \\ \pi & \text{x-direction first} \\ -\pi & \text{y-direction first} \end{cases} \tag{39}$$

In the first case, the symmetry of the summation is taken to be either a circular or square shell, retaining the symmetry between x- and y-directions. In the second and the third, the summation shell is a strip along x- and y-directions, respectively. In addition to this convergence issue, we also note that the potential for a unit dipole in the form of Eq. (35) where the last term is replaced by Eq. (36) is not periodic for any value of S_2. The treatment of the term, therefore, depends on the physics of the problem under consideration. Thus, we separate the term that contains $\tilde{S}_2$. Since for the geometry we consider $\tilde{S}_m$ are zero for odd m,

$$w_\psi(z) = \sum_{j=1}^{N} \mu_j \left(\frac{1}{z_j - z} + \sum_k{}' \frac{1}{z_j - z + \zeta_k} + \sum_{m=1}^{\infty} \tilde{S}_{2m+2}(z - z_j)^{2m+1} + \tilde{S}_2(z - z_j) \right). \tag{40}$$

The problem of conditional convergence in computing the potential in periodic cells has been studied in the context of the electrostatic energy in ionic crystals. We follow a similar approach suggested by Smith [27], and replace the last term in Eq. (40) with a shape-dependent dipole correction term, which can be determined given the shape of the unit cell. Rather than calculating this term via a complicated analytic method, we will take advantage of the linearity of the term to impose periodicity. We now limit our discussion to the case where the unit cell is square. (The corresponding details for the parallelogram-shaped unit cell needed in calculating the elastic field are given later in Section 5.2.) For the square unit cell, we consider a region defined by four corners $(-\frac{1}{2}, -\frac{1}{2})$, $(-\frac{1}{2}, \frac{1}{2})$, $(\frac{1}{2}, -\frac{1}{2})$, and $(\frac{1}{2}, \frac{1}{2})$. Without loss of generality, we take two pairs of translationally equivalent points (cf. Fig. 1), and calculate the potential (excluding the term containing $\tilde{S}_2$) at these points. To calculate a unit dipole correction, consider a dipole of unit strength ($\mu = 1$) at the origin for simplicity. Let $\upsilon(z)$ be the potential generated by the dipole excluding the conditionally convergent term,

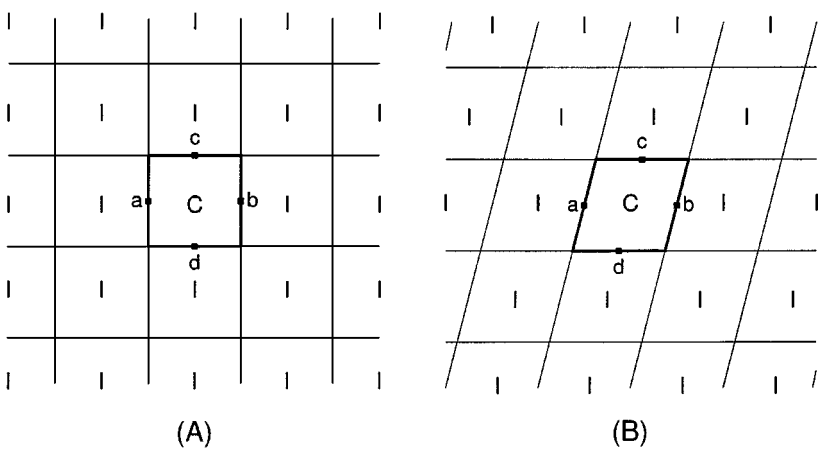

FIG. 1. Example definition of translationally equivalent points, (A) for the square unit cell (for calculation of the diffusion field) and (B) for the parallelepiped unit cell (for calculation of the elastic field). C and I denote the central unit cell and repeated image cells, respectively. Points a and b are an example of a translationally equivalent pair in the x-direction, while c and d are one in the y-direction.

$$\upsilon(z) = \frac{1}{-z} + \sum_k{}' \frac{1}{\zeta_k - z} + \sum_{m=1}^{\infty} \tilde{S}_{2m+2} z^{2m+1}. \tag{41}$$

We suggest the dipole correction term in the form

$$w_\phi^{dc}(z) = -\sum_{j=1}^{N} \left(\Re(\mu_j C_x)(x - x_j) + \Re(\mu_j C_y)(y - y_j) \right), \tag{42}$$

so that

$$\begin{aligned} w_\psi(z) \;=\; & \sum_{j=1}^{N} \left\{ \mu_j \left(\frac{1}{z_j - z} + \sum_k{}' \frac{1}{z_j - z + \zeta_k} + \sum_{m=1}^{\infty} \tilde{S}_{2m+2} (z - z_j)^{2m+1} \right) \right. \\ & \left. - \left[\Re(\mu_j C_x)(x - x_j) + \Re(\mu_j C_y)(y - y_j) \right] \right\}, \end{aligned} \tag{43}$$

where C_x and C_y are the difference of υ at the translationally equivalent points in the x- and y-directions, respectively,

$$\begin{aligned} C_x &= \upsilon(0.5 + 0i) - \upsilon(-0.5 + 0i), \\ C_y &= \upsilon(0 + 0.5i) - \upsilon(0 - 0.5i). \end{aligned}$$

Here, the translationally equivalent points are taken to be $z = \pm 0.5$ and $z = \pm i 0.5$ as shown in Fig. 1. It should be noted that C_x and C_y can be complex numbers. Evaluating numerically C_x and C_y for the square unit cell, we have

$$C_x = -\pi, \tag{44}$$

$$C_y = i\pi. \tag{45}$$

Therefore, we have for a potential resulting from dipoles in periodically arranged two-dimensional square unit cells in the absence of an applied field,

$$w_\psi(z) = \sum_{j=1}^{N} \left(\sum_k{}''' \frac{\mu_j}{z_j - z + \zeta_k} + \sum_{m=1}^{\infty} \mu_j \tilde{S}_{2m+2} (z - z_j)^{2m+1} + \pi \mu_j^* (z - z_j) \right), \tag{46}$$

where the conditionally convergent term has been replaced with a dipole correction term, $w_\psi^{dc}(z, z_j)$. The term $\sum'''$ denotes summation over k for the nearby cells and the cell at the center (i.e., over the nonwell-separated cells).

Similarly, we now calculate a corresponding expression for the potential generated by monopoles. A straightforward expansion together with charge neutrality (which for the diffusion problem ensures that the area fraction of particle phase remains constant) gives

$$\begin{aligned} w_\phi(z) = & \sum_{j=1}^{N} q_j \left\{ \sum_k{}''' \log(z_j - z + \zeta_k) \right. \\ & \left. - \sum_{m=1}^{\infty} \left(\frac{\tilde{S}_{2m+2}}{2m+2} (z - z_j)^{2m+2} \right) - \frac{\tilde{S}_2}{2} (z - z_j)^2 \right\}. \end{aligned} \tag{47}$$

Again, the conditionally convergent term is separated from other terms, and is replaced by the dipole correction term. That is,

$$w_\phi(z) = w_\phi^{ac}(z) + w_\phi^{dc}(z), \tag{48}$$

where

$$w_\phi^{ac}(z) = \sum_{j=1}^{N} q_j \left\{ \sum_k{}''' \log(z_j - z + \zeta_k) - \sum_{m=1}^{\infty} \left(\frac{\tilde{S}_{2m+2}}{2m+2} (z - z_j)^{2m+2} \right) \right\} \tag{49}$$

is the absolutely convergent part. The dipole correction term, w_ϕ^{dc}, can be determined by noticing that

$$w_\psi = \frac{\partial w_\phi}{\partial n_j}, \tag{50}$$

if $\mu_j = q_j(n_{xj} + i n_{yj})$. Thus, integrating the dipole correction term for the potential generated by a dipole results in the dipole correction term for the potential generated by a monopole. Therefore, for each j we compute the integral

$$w_{\phi j}^{dc}(z, z_j) = \int_0^{z_j} \pi \mu_j^*(z - z_j')\, dn_j'. \tag{51}$$

Again using Eqs. (31) and (32),

$$w_{\phi j}^{dc} = \pi q_j \left[\int_0^{x_j} (z - z_j')\, dx_j' - i \int_0^{y_j} (z - z_j')\, dy_j' \right] = -\frac{\pi q_j}{2} (z_j - 2z) z_j^*. \tag{52}$$

Note the correction includes a constant term (independent of z) that does not affect the derivative of the potential, as well as a term that is linear in z. A potential calculated using the correction term given in Eq. (52) is periodic in its real part. Notice also it is analytic in z since it satisfies the Cauchy–Riemann equations. The formula for periodic monopole potential in a two-dimensional square unit cell in the absence of an applied field is therefore given by

$$w_\phi(z) = \sum_{j=1}^{N} q_j \left[\sum_k{}''' \log(z_j - z + \zeta_k) - \sum_{m=1}^{\infty} \frac{\tilde{S}_{2m+2}}{2m+2} (z - z_j)^{2m+2} - \frac{\pi}{2} (z_j - 2z) z_j^* \right]. \tag{53}$$

The same procedure can be carried out for the case of unit cells with different shapes. With C_x and C_y determined numerically, the resulting expression is given by

$$\begin{aligned} w_\phi(z) = \sum_{j=1}^{N} q_j \Bigg(& \sum_k{}''' \log(z_j - z + \zeta_k) - \sum_{m=1}^{\infty} \frac{\tilde{S}_{2m+2}}{2m+2} (z - z_j)^{2m+2} \\ & - \left[C_x^R x_j \left(x - \frac{1}{2} x_j \right) + C_y^R (y - y_j) x_j - C_x^I y_j (x - x_j) - C_y^I y_j \left(y - \frac{1}{2} y_j \right) \right] \Bigg), \end{aligned} \tag{54}$$

where the superscripts R and I denote the real and imaginary part, respectively.

We have now formulae for potentials in a periodically arranged cell, which allow us to calculate potentials using the fast multipole method. Equations (46) and (53) are used in solving the diffusion problem.

We find that the potentials using the Fourier method and the new method always agree. This result is illustrated in the simple case of two monopoles in a square unit cell for simplicity. Consider a square unit cell of area 1 whose center is located at the origin. The unit cell contains a positive charge of strength 1 located at $z_1 = x_1 + iy_1$ and a negative charge of strength -1 located at $z_2 = x_2 + iy_2$. As before, the unit cell is periodically arranged to fill the space so that the potential generated by the charges is periodic. In this case, Eq. (53), along with the fact that $\tilde{S}_m$ for $m \geq 4$ are zero for all m except $m = 4l$, reduces to

$$w_\phi(z) = \log \frac{(z_1 - z)^9 + 3(z_1 - z)^5 - 4(z_1 - z)}{(z_2 - z)^9 + 3(z_2 - z)^5 - 4(z_2 - z)} + \sum_{m=1}^{\infty} \frac{\tilde{S}_{4m}}{4m} \left(-(z - z_1)^{4m} + (z - z_2)^{4m}\right) - \frac{\pi}{2}\left((z_1 - 2z)z_1^* - (z_2 - 2z)z_2^*\right). \tag{55}$$

For comparison, the potential computed using the Fourier method is given by

$$\phi(\mathbf{x}) = \sum_{\mathbf{k}, |\mathbf{k}| \neq 0} -\frac{1}{(2\pi |\mathbf{k}|)^2} \sum_{j=1}^{2} q_j \exp(2\pi i \mathbf{k} \cdot (\mathbf{x} - \mathbf{x}_j)), \tag{56}$$

where $\mathbf{k}$ is the wave number vector and $\mathbf{x}_j = (x_j, y_j)$. Figure 2 shows the potentials

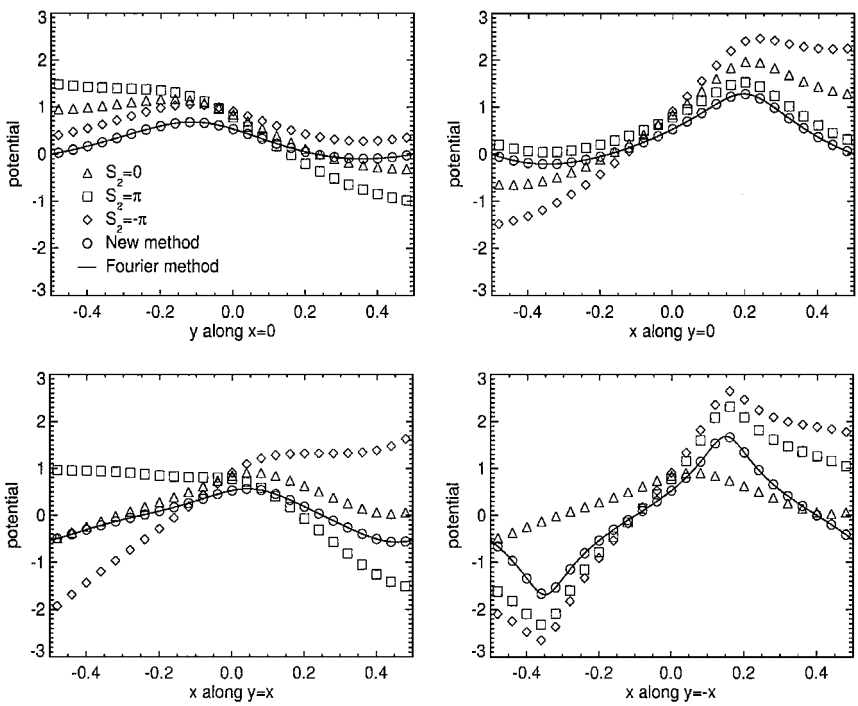

FIG. 2. The potential along $x = 0$, $y = 0$, $y = x$, and $y = -x$ using various expressions for a system of two charges, $q = +1$ at $(x, y) = (-0.4, 0.3)$ and $q = -1$ at $(x, y) = (0.2, -0.1)$. The potential agrees with the periodic potential calculated using Fourier method only if the conditionally convergent term is replaced by the dipole correction term.

computed using Eqs. (54) and (56) for $(x_1, y_1) = (-0.4, 0.3)$ and $(x_2, y_2) = (0.2, -0.1)$, as well as those calculated by Eq. (47) using S_2 given by Eq. (39). It is clear that the potential calculated by the new formula is in agreement with that of the Fourier Method. This demonstrates the periodicity of the new formulation for the monopole potential (and thus the dipole potential) in a periodically arranged cell calculated in physical space required for the diffusion and elasticity problems.

The above formulae are correct for the case where the unit cell, or the unit region of integration, is square. We will note in Section 5.2 that the transformation used in the multipole expansion for the elastic field requires a different formulation since the unit cell is not square.

5. IMPLEMENTATION OF THE FAST MULTIPOLE METHOD

5.1. Boundary Integral Method for Diffusion Problem

For details of the FMM itself, we refer the readers to the original paper [11]. We apply the FMM to solve the boundary-value problem for diffusion. Following [10], we discretize each boundary, γ^j into N_j points, and the total number of distinct boundaries is M. Thus, the total number of mesh points is $N = \sum_{j=1}^{M} N_j$. We solve Eq. (5) subject to the boundary conditions Eq. (6) and mass conservation. The interfaces are updated in time using Eq. (8). The normal derivative in Eq. (8) can be expressed in terms of the tangential derivative along the interface, using the Cauchy–Riemann relation [22],

$$\frac{\partial u}{\partial n} = \frac{\partial v}{\partial s}, \tag{57}$$

where v is the harmonic conjugate function of u.

Following [10], we seek a solution of Eqs. (5) and (6) in the form

$$u(\mathbf{x}) = \frac{1}{2\pi} \sum_{j=1}^{M} \int_{\gamma^j} \mu(\mathbf{x}') \frac{\partial \log |\mathbf{x}' - \mathbf{x}|}{\partial n'} \, dx' + \frac{1}{2\pi} \sum_{j=1}^{M} \int_{\gamma^j} \mu(\mathbf{x}') \, dx' + \sum_{j=1}^{M} A^j \log \left| \mathbf{x} - \mathbf{x}_{int}^j \right|, \tag{58}$$

where $\mathbf{x}_{int}^j$ is a point interior to γ^j, taken to be the center of the j-th particle. The following constraints are then imposed,

$$\sum_{j=1}^{M} A^j = 0, \tag{59}$$

$$\int_{\gamma^j} \mu(\mathbf{x}) \, dx = 0 \quad \text{for } j = 1, \ldots, M-1, \tag{60}$$

$$\mu(\mathbf{x}_0) - \frac{1}{\pi} \sum_{j=1}^{M} \int_{\gamma^j} \mu(\mathbf{x}) \left[\frac{\partial \log |\mathbf{x} - \mathbf{x}_0|}{\partial n} + 1 \right] dx - 2 \sum_{j=1}^{M} A^j \log \left| \mathbf{x}_0 - \mathbf{x}_{int}^j \right| = -2 f(\mathbf{x}_0), \tag{61}$$

where $\mathbf{x}_0$ is a point on the boundary, and $f(\mathbf{x}_0)$ is the boundary condition, $u(\mathbf{x}_0)$. Equations (58)–(61) have a unique solution. Since these integrals are over the interfaces,

we need to discretize only the interfaces. To ensure high accuracy, we use 128 to 4096 mesh points over the interfaces, which are spaced equally over an interface of a particle, but the number of mesh points is adaptive in time for each individual particle to respond to the change in the strength of the elasticity and the proximity to the interfaces of other particles.

The discretization of Eqs. (58)–(61) results in a matrix equation of the form

$$\begin{pmatrix} I-K & B \\ C & D \end{pmatrix}\begin{pmatrix} \boldsymbol{\mu} \\ \mathbf{a} \end{pmatrix} = \begin{pmatrix} -2\mathbf{f} \\ 0 \end{pmatrix}, \tag{62}$$

where I is the N by N identity matrix; K is an N by N matrix that represents double layer interactions; B is an N by M matrix that represents the coupling of the logarithmic terms; C and D, M by N and M by M matrices, respectively, result from the constraints in Eqs. (59)–(61). The column vectors $\boldsymbol{\mu}$, $\mathbf{a}$, and $\mathbf{f}$ take the values of unknown double layer density μ_i, unknown coefficients A^j, and the boundary conditions, f_i, where $i = 1, N$ and $j = 1, M$. The equations are solved using the generalized minimal residual method (GMRES) [25], since a good preconditioner exists [10]. We use the FMM as described in [10] for evaluating the matrix–vector multiplication required in this process. The number of required iterations depends on factors such as the particle spatial distribution, but is typically about 20 to achieve a relative residual error of 10^{-8}.

5.2. Calculation of the Elastic Field

The FMM is generally readily adoptable for the cases where the Green's function has the form

$$G(z, z') = \log(z' - z), \tag{63}$$

or its derivative, since an expansion in multipole moments is straightforward. However, the Green's function for linear anisotropic elasticity is not in this form. Specifically, the derivative of the Green's function when $\mathbf{n} = (1, 0, 0)$ and $\mathbf{m} = (0, 1, 0)$ follows from Eq. (18),

$$\begin{aligned} g_{jk,l}(\mathbf{x}, \mathbf{x}') &= \frac{-1}{2\pi i}\sum_{\alpha=1}^{6} \pm A_{j\alpha}A_{k\alpha}\frac{\delta_{1l} + \lambda_\alpha\delta_{2l}}{(x - x') + \lambda_\alpha(y - y')} \\ &= \frac{-1}{2\pi i}\sum_{\alpha=1}^{6} \pm A_{j\alpha}A_{k\alpha}\frac{\delta_{1l} + \lambda_\alpha\delta_{2l}}{(x - x') + a_\alpha(y - y') + ib_\alpha(y - y')}, \end{aligned} \tag{64}$$

where a_α and b_α are the real and imaginary parts of λ_α, respectively.

In order to use the FMM, we introduce a new variable

$$z_\alpha = (x + a_\alpha y) + ib_\alpha y. \tag{65}$$

Using z_α, Eq. (64) becomes

$$g_{jk,l}(\mathbf{x}, \mathbf{x}') = \frac{-1}{2\pi i}\sum_{\alpha=1}^{6} \pm A_{j\alpha}A_{k\alpha}\frac{\delta_{1l} + \lambda_\alpha\delta_{2l}}{z_\alpha - z'_\alpha}. \tag{66}$$

Now the Green's function is easily expandable in powers of $(z_\alpha - z'_\alpha)$, and the FMM can be applied on the z_α plane.

However, the shape of the unit cell in the z plane is no longer the same as the original shape. For example, corners of the original square unit cell are transformed to

$$\begin{aligned}(s, s) &\to (s + a_\alpha s, b_\alpha s)\\ (-s, s) &\to (-s + a_\alpha s, b_\alpha s)\\ (-s, -s) &\to (-s - a_\alpha s, -b_\alpha s)\\ (s, -s) &\to (s - a_\alpha s, -b_\alpha s).\end{aligned} \tag{67}$$

Thus, a square unit cell is preserved only when $a_\alpha = 0$ and $b_\alpha = 1$. When the dimensionless elastic constants are given by $c_{11} = 1.98$ and $c_{12} = 1.18$ ($c_{44} = 1$ by definition), as in the case for Ni, one of the eigenvalues is given by $a = 0.69$, $b = 0.72$ (see Eq. (23)). For this case, a square unit cell is transformed to a parallelogram which has corners at

$$(0.845, 0.36), (-0.155, 0.36), (-0.845, -0.36), (0.155, -0.36). \tag{68}$$

The distance from the center of the cell to the furthest corner (0.845, 0.36) is 0.918 (as opposed to 0.707 in the case of a square unit cell). The distance from the center to the closest corner $(-0.155, 0.36)$ is 0.392. Since these two distances are significantly different, we must modify the definition of "well-separated cells."

Let d_j be the distance from the center of the cell at the origin to the center of the cell j. Define $c = (d_j - d)/r$, where d is the distance to the furthest corner from the center of a unit cell. In this particular example, $d = 0.918$. Using the definition of well-separated cells given by Greengard and Rokhlin for a square unit cell, we take $c > 2$ as the condition for well-separated cells.

Figure 3 shows the well separated cells in relation to the center cell. In the FMM procedure, a unit cell is also divided into subcells to apply the multipole expansion. The same criteria described above is also applied when defining neighboring cells and well-separated cells within the unit cell.

In Section 4, we deferred the discussion of calculating the periodic elastic field. In this case, the formulae must account for the nonsquare shape of the unit cell. Again, all $\tilde{S}$'s but $\tilde{S}_2$ can be computed using the renormalization method [6]. In doing so, however, attention should be given to the change of the definition of "well-separated cell," as well as that of the shape of the cell, both of which modify the value of $\tilde{S}$'s. The translationally equivalent

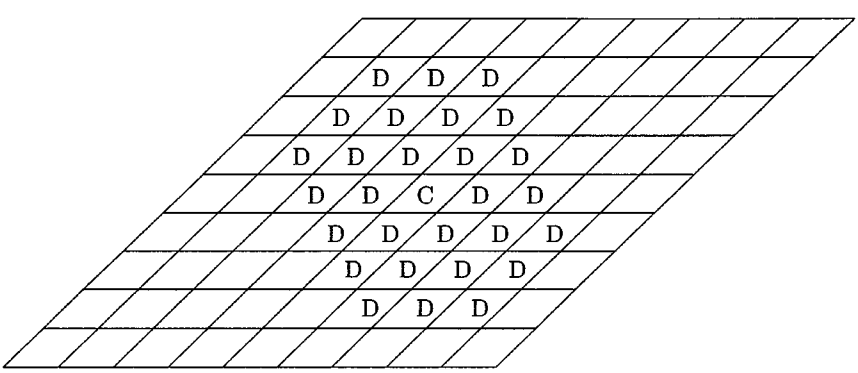

FIG. 3. Definition of well-separated cells for the parallelogram-shaped unit cell for $a = 0.69$ and $b = 0.72$. C and D denote the cell at the center and nearby (not well-separated) cells, respectively. The blank cells are well separated from center cell. The shape of the unit cell is approximate.

points must be adjusted according to the shape of the unit cell, also (cf. Fig. 1). For C_x and C_y, we have

$$C_x = \upsilon(0.5 + 0i) - \upsilon(-0.5 + 0i), \tag{69}$$

$$C_y = \upsilon(0.5a_\alpha + 0.5b_\alpha i) - \upsilon(-0.5a_\alpha - 0.5b_\alpha i), \tag{70}$$

where υ is defined in Eq. (41), and Eq. (43) remains valid. Note that in Eq. (43) for the parallelogram system x and y are not equal to $\Re(z)$ and $\Im(z)$. Rather, x and y refer to the Cartesian coordinates before the transformation; that is

$$\begin{aligned} x &= \Re(z_\alpha) - a_\alpha \Im(z_\alpha)/b_\alpha \\ y &= \Im(z_\alpha)/b_\alpha. \end{aligned} \tag{71}$$

6. θ-L FORMULATION

6.1. Formulation

One problem that is commonly encountered in advancing the interface via Eq. (8) is the stiff time stepping. A simple linear stability analysis yields the condition for stability,

$$\Delta t \le K(\Delta x)^3, \tag{72}$$

where Δx is the minimum spacing between points on the interface, and K is a constant. Since the time step varies as $(\Delta x)^3$, explicit time stepping is very expensive. To remove the stiffness, we adopt the small-scale decomposition technique, or the θ-L formulation, introduced by Hou, Lowengrub, and Shelly [13]. Below we summarize the method briefly, and refer the readers to the original reference for more details.

Consider a particle interface, γ, that is described by a set of points $\mathbf{x}(\alpha, t)$, where α parameterizes the curve. The evolution of γ is prescribed by the normal velocity V. Instead of evolving the coordinate of the i-th boundary point of the j-th particle, (x_i^j, y_i^j), we keep track of the center of mass coordinate (x_c^j, y_c^j), the total arc length l^j, and the angle θ_i^j between the tangential vector at the interface at the i-th point and the x-axis. The center of mass is updated by advancing the interfacial points explicitly with normal and tangential velocities and calculating the center of mass from the new interfacial points. Using the sign and direction convention consistent with [13], the evolution of the total arc length and the shape is given by

$$\frac{\partial l^j}{\partial t} = -\frac{1}{l^j} \int_0^{2\pi} \frac{\partial \theta^j}{\partial \alpha'} V^j(\alpha')\, d\alpha', \tag{73}$$

$$\frac{\partial \theta^j}{\partial t} = \frac{2\pi}{l^j} \left[\frac{\partial V^j(\alpha)}{\partial \alpha} + \frac{\partial \theta^j(\alpha)}{\partial \alpha} T^j \right]. \tag{74}$$

Here, T^j is the tangential velocity introduced to keep the spacing of the boundary points constant and is given by

$$T^j(\alpha, t) = T^j(0, t) + \int_0^\alpha \frac{\partial \theta^j}{\partial \alpha'} V^j(\alpha')\, d\alpha' - \frac{\alpha}{2\pi} \int_0^{2\pi} \frac{\partial \theta^j}{\partial \alpha'} V^j(\alpha')\, d\alpha', \tag{75}$$

where the arbitrary change of frame, $T^j(0,t)$, is taken to be 0. Equation (73) is not limited by the stability condition of Eq. (72). On the other hand, Eq. (74) is subject to the stability condition since it describes the change in the shape of the curve, which is the source of the stiffness. The stiffest part of Eq. (74) is linearizable in Fourier space. We found that the following scheme works best to stabilize the time advance while minimizing smoothing,

$$\frac{\partial \hat{\theta}^j(t,k)}{\partial t} = -\frac{1}{2}\left(\frac{2\pi}{l^j}\right)^3 |k|^3 \hat{\theta}^j(t,k) + \hat{N}^j(t,k), \tag{76}$$

where

$$N^j(\alpha,t) = \frac{2\pi}{l^j}\left(\frac{\partial V^j}{\partial \alpha} + \frac{\partial \theta^j}{\partial \alpha} T^j\right) - \frac{1}{2}\left(\frac{2\pi}{l^j}\right)^3 \mathcal{H}\left[\frac{\partial^3 \theta^j}{\partial \alpha^3}\right]; \tag{77}$$

the hat denotes the Fourier transform, $\mathcal{H}$ is the Hilbert transform, and k is the wave number. In this form, an implicit discretization of the first term on the right-hand side is straightforward, enabling us to avoid the time-step constraint. We discretize Eq. (76) using the following scheme,

$$\frac{\hat{\theta}_i^j(t+\Delta t,k) - \hat{\theta}_i^j(t,k)}{\Delta t} = -\frac{1}{2}(2\pi)^3 |k|^3 \left[\frac{\hat{\theta}_i^j(t+\Delta t,k)}{(l^j(t+\Delta t))^3} + \frac{\hat{\theta}_i^j(t,k)}{(l^j(t))^3}\right] + \hat{N}^j(t,k), \tag{78}$$

and Eq. (73) using first-order explicit scheme,

$$\frac{l^j(t+\Delta t) - l^j(t)}{\Delta t} = F^j(t), \tag{79}$$

where $F^j(t)$ represents the right-hand side of Eq. (73) for the j-th particle at time t. In equilibrium (i.e., when $\hat{\theta}^j(t+\Delta t,k) = \hat{\theta}^j(t,k)$), Eq. (78) satisfies the necessary condition that the sum of the two terms in the right-hand side must vanish as the right-hand side of Eq. (76) becomes zero. Note the interfacial length l^j is updated via Eq. (73) before the shape is updated. This is required by the fact that $l^j(t+\Delta t)$ appears in Eq. (78). Higher-order schemes for shape update have been suggested for the above time integration [14, 18]. However, we have chosen to use the schemes described above because some particles may disappear during a time step in our simulation, which may cause a large, local, artificial change in the concentration from one time step to the next. Thus, using the value of normal velocity from the previous time step may have adverse effects. We take the mesh spacings to be constant in α on an individual body during the update step, although they are adaptively refined or coarsened during the evolution to assure adequate resolution and optimal efficiency.

6.2. Time Step for Diffusion Problem with Elasticity

The θ-L formulation removes the stiffness from the curvature part of the boundary condition. If the interfacial motion is driven only by curvature, the method works quite well as such motion tends to smooth out high curvature regions. However, in our case the elastic stress can also drive the interfacial motion. We found that the time step that is appropriate for the interfacial-energy-driven case can cause significant inaccuracy in systems with large

stress effects. In particular, the changes in the shapes were underestimated at locations where elastic stress was strong. To remedy this, we introduced a second-level time step, Δt_2, such that

$$\Delta t_2 = \Delta t / N_{loop}, \tag{80}$$

where Δt is the first-level time step, as used in the θ-L formulation, which must be reduced as the stress effects increase, and N_{loop} is the number of loops over the implicit time stepping of the shapes, as given by Eq. (78), within one first-level time step. During one first-level time step, $V^j(\alpha)$ is fixed while the shape is evolved via Eq. (78) using intermediate values of l^j. The term N_{loop} should be as large as possible without causing significant change in the normal velocity so that the first-level time step can be as large as possible while minimizing errors. Fortunately, the potentials are not very sensitive to changes in the shapes of particles. We take N_{loop} to be 100, which worked best in our test runs. We also made extensive test runs for the first-level time step. We find the following dimensionless time-step size optimizes the balance between numerical convergence and efficiency,

$$\Delta t = \frac{\langle r \rangle^3}{\langle r_0 \rangle^3} \mathrm{Max}[6 \cdot 10^{-3} \exp(-0.5756 \langle L \rangle), 2.5 \cdot 10^{-4}], \tag{81}$$

where $\langle L \rangle$ is the system's average L defined in Eq. (7), $\langle r \rangle$ is the average radius, and $\langle r_0 \rangle$ is the initial average radius of particles. Note for high $\langle L \rangle$, Δt can be as small as $2.5 \cdot 10^{-4}$, making the second-level time step, $\Delta t_2 = 2.5 \cdot 10^{-6}$, almost as small as the time step required by the explicit time stepping. This requirement is a direct result of the high angular dependence of the elastic field and the resulting growth of the higher-order terms that are truncated in Eq. (78) [18]. In the absence of stress, Δt of $2.5 \cdot 10^{-3}$ was adequate without the use of the second-level time step [2]. By adopting the second-level time step, we were able to decrease the computation time by two orders of magnitude.

Leo, Lowengrub, and Nie have suggested a different time-step scheme in their recent paper [18]. We are currently examining the scheme to determine whether it is appropriate in our calculation. Their suggestion may further improve the performance of the code.

7. NUMERICAL SIMULATION

Combining all of the methods outlined above yields the following procedure:

1. Initialization: set up initial sets of interfaces and initialize variables.
2. Set the first-level time step, Δt, as a function of $\langle L \rangle$ (see Eq. (81)).
3. Determine the elastic field along the interfaces of the particles.
4. Calculate the boundary conditions on the interfaces.
5. Solve the diffusion equation with the above boundary conditions.
6. Calculate the harmonic conjugate function and the normal velocity.
7. Update the location of the center of mass.
8. Update the interfacial arc lengths of the particles.
9. Using the second-level time step ($= \Delta t / N_{loop}$), update the shapes of particles via the tangent angle using the intermediate values of the total interfacial arc lengths. Repeat N_{loop} times while holding the normal velocity fixed.

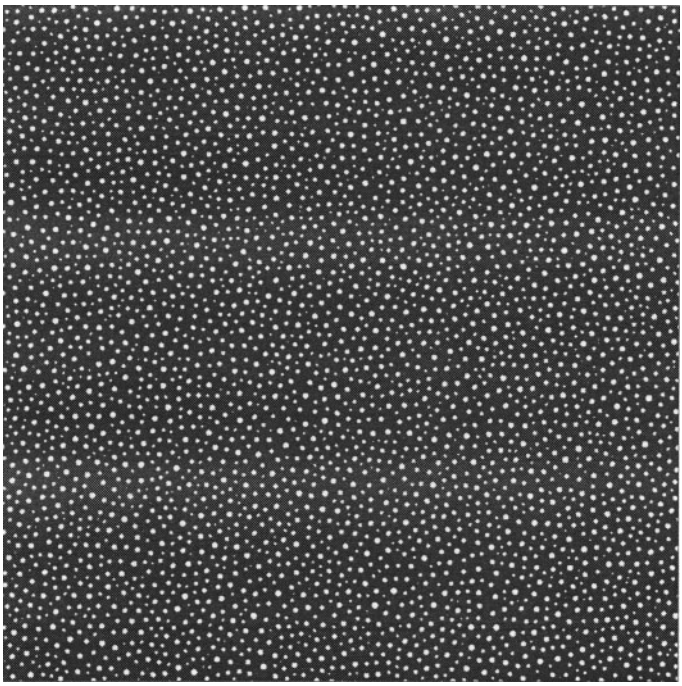

FIG. 4. The initial microstructure, consisting of 4000 circular particles. The box corresponds to the computational domain.

10. Using the center-of-mass locations from Step 7, the interfacial lengths from Step 8, and the shapes from Step 9, calculate the updated locations of interfacial points.
11. Repeat Steps 2–10.

A multiparticle system containing various sizes of particles will not reach an equilibrium state because of the diffusion of mass between the particles. We start our calculations using 4000 circular particles (see Fig. 4). In Fig. 5, we show the time sequence of the microstructural evolution of a system with $\langle L_0 \rangle = \langle L(t = 0) \rangle = 1$. Extensive quantitative analyses of the results are performed, and are published elsewhere [32, 33]. Here we focus on the qualitative nature of the results.

When only one particle exists in the system, a particle evolves toward its equilibrium shape, which depends on the parameter, L. The equilibrium shapes of an isolated particle have been computed for a Ni-Al system by Thompson, Su, and Voorhees [30]. They found that the shape is a circle when $L = 0$ and becomes a four-fold symmetric square-like shape as L increases. When L exceeds the critical value 5.6, a bifurcation takes place and two-fold symmetric (elongated) shapes become the energy-minimizing equilibrium shapes. In our multiparticle simulation, we observe a similar behavior. When elastic stress is negligible, the particles are circular (or nearly circular). During coarsening in many-body systems, however, the shapes of the particles do not reach equilibrium, but rather the mass diffusion from surrounding particles and interparticle elastic interactions cause the shapes to be slightly distorted from the equilibrium shape.

The particles become nearly four-fold symmetric shapes, even at a low $\langle L \rangle$ of 2.0. A magnification view (5x) is provided in Fig. 5, top right, to show the shape variation: smaller particles maintain nearly circular shapes while larger particles tend to achieve more

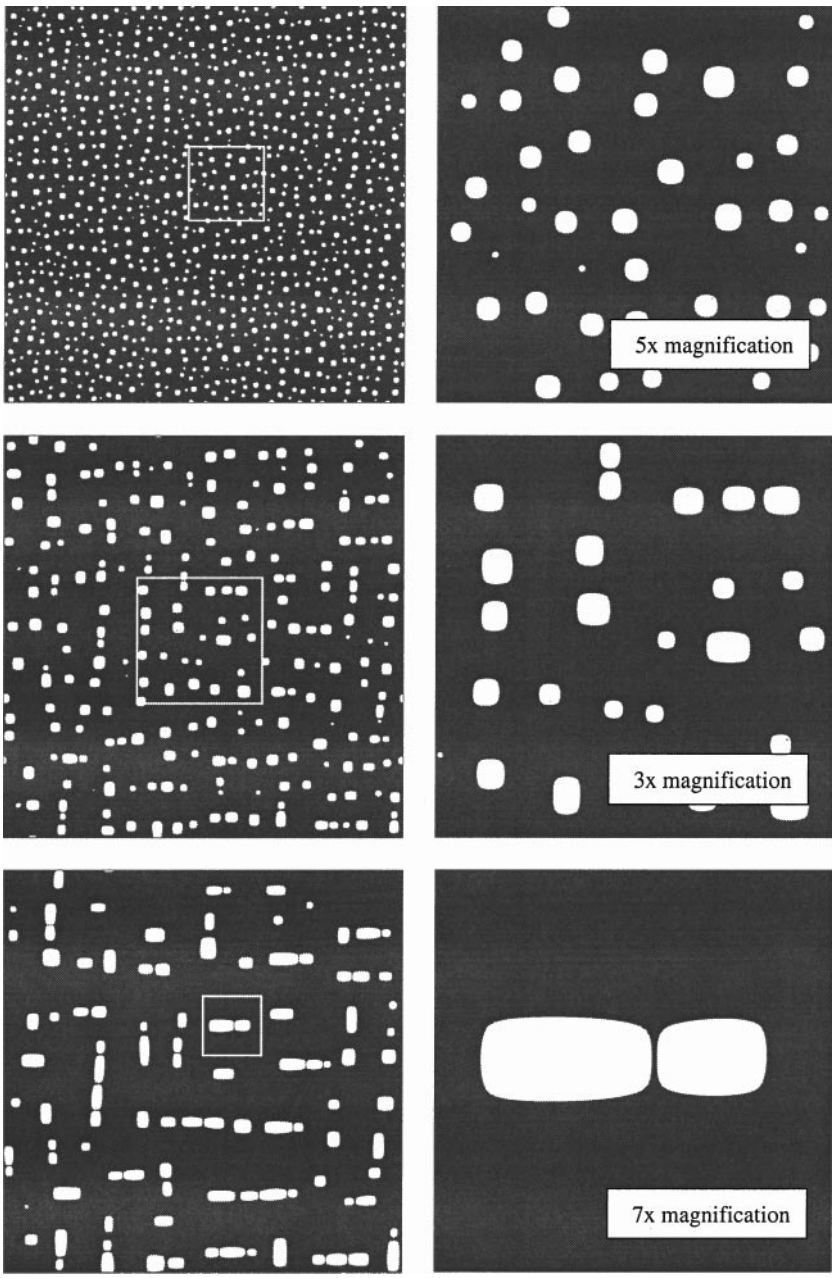

FIG. 5. The microstructures over the computational domain (left) and selected regions magnified from corresponding microstructure. The values of $\langle L \rangle$ are 2.0, 4.1, and 6.1, corresponding to $t = 13.5$, 152.2, and 512.1, from the top to the bottom. The number of remaining particles are 1066, 229, and 104, respectively. The magnified regions are noted by boxes with white outline on the left.

four-fold, square-like shapes. In addition, we find particle alignment along the vertical and the horizontal directions which correspond to the elastically soft $\langle 100 \rangle$ directions of the crystal. The shape changes of the particles are mainly due to the elastic energy generated by the particle itself, rather than by the elastic interaction, and the particle alignment is due to the configurational forces (or equivalently elastic interaction energy) generated by other

particles [28]. An exception to this is when two particles or more are very close; then the elastic interactions can cause the shapes to be distorted significantly.

Although the effects of elastic self-energy are obvious from the shape change, the alignment of particles is not as clear at $\langle L \rangle = 2$. This is likely to be because the elastic interaction energy is typically a small fraction of the total elastic energy at the low area fraction we are examining. However, early signs are seen where chains establish themselves by chance as a result of fluctuations in the initial configuration. Elastic interaction helps to stabilize such conformations, and they survive for a long period of time at the expense of particles not aligned with others.

By $\langle L \rangle = 4.1$, most particles are aligned with several others, making the microstructure consist of more ordered congregations of chains. Particles in the middle of chains are stabilized by the elastic interaction energy, and they may grow even if they are smaller than the surrounding particles. In addition, a chain may grow as a whole at the expense of isolated large particles or smaller chains. Slight elongation (a non-four-fold shape) seen in many particles is due to three factors: (1) large particles have $L > 5.6$ and two-fold shapes have lower energy in that case, (2) the elastic interaction with another particle causes the particle to elongate itself along the axis of alignment, and (3) aligned particles growing at the expense of close neighbors do so by extending themselves toward these neighbors. Again, a magnified view (middle right in Fig. 5) shows the shape changes. As a result of particle migration and preferential growth, particle interfaces may become very close to that of their immediate neighbors. It may seem that some of the interfaces of particles are touching or connected. However, as shown in the 7x magnified view at $\langle L \rangle = 6.1$ (bottom right in Fig. 5), the separations between interfaces are maintained and well resolved even at this late stage. The separation is maintained throughout the runs by the elastic repulsion between particles that occurs at a short distance. Using the materials parameter of Ni-Al, this separation is large on an atomic scale, and thus coalescence is not important for this system for the range of $\langle L \rangle$ studied. It should be noted, however, that coalescence may become a major effect at a higher volume fraction and/or a larger $\langle L \rangle$. Although we do not allow coalescence in these simulations, we are currently studying a possibility of a hybrid method that allows for both high resolution of particle shapes (as in these simulations) and coalescence.

All of these observations are consistent with experimental findings and previous numerical simulations. However, using an initial number of particles as large as 4000, we are now able to make systematic characterizations of the resulting microstructure to allow quantitative comparisons to experiments.

Through the analysis of our calculations, we identified various aspects of underlying processes in complex systems with free interfaces and elastic effects [32, 33]. The analyses of the calculation results for the case shown above revealed a system that was simpler than we expected. One such finding was the change in the kinetics of coarsening in these systems. Using the results, we were able to suggest a new simple picture of coarsening that depends only on the symmetry of particle shapes. Although our calculations are limited to two dimensions, the information we obtained will help us understand the effects of elastic stress on the coarsening processes in real (3D) systems.

8. PERFORMANCE

For 4000-particle runs, one time step takes up to 500 CPU seconds on an NEC NX-4. As coarsening reduces the number of particles, the computational time decreases significantly.

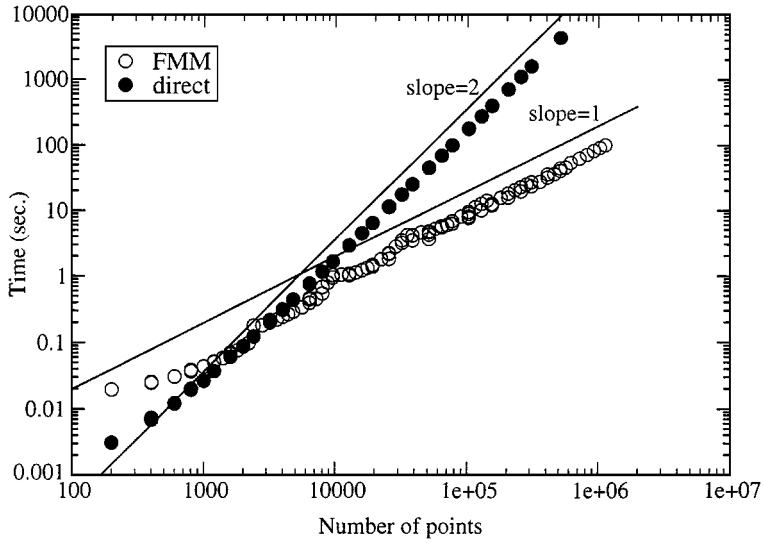

FIG. 6. The computational time for calculating the elastic field is plotted against number of points in the computational domain on a log-log scale. Lines with slopes 1 and 2 are provided to guide the eye.

The total number of time steps required for a complete run depends strongly on $\langle L_0 \rangle$, because of the dependence of the time step on the strength of elasticity. For $\langle L_0 \rangle = 1$ case, the total CPU time was approximately 18 days. Up to 4000 particle runs are manageable on workstations with current technology, such as a Hewlett Packard 9000/785, over 10 days to six weeks, depending on $\langle L_0 \rangle$.

We summarize the comparison of performance between the direct sum method (DSM) and the FMM for the calculation of the elastic field in Fig. 6. The DSM code uses a simple direct sum to calculate the elastic field via Eq. (13). For this reason, we assume that the computational domain is isolated (nonperiodic). The FMM code calculates the potential via Eq. (66) using the FMM modified for the parallelogram-shaped unit cell (without including the periodicity). Each point on the plot represents a result from a run. The number of particles, M, in a run was varied from 50 to 550, while the number of mesh points on each particle, n, is varied from 4 to 2048. The tests were performed only for the purpose of benchmarking, and we disregard the fact that some of the resolution settings are not adequate to obtain accurate results. The computational time, T_c, for calculating the elastic field for a given configuration is plotted against the total number of mesh points, $N = Mn$, on a log–log scale to show the scaling of T_c with N. Lines with slopes 1 and 2, which are indicative of $O(N)$ and $O(N^2)$ behavior, respectively, are plotted also to guide the eye.

For a small total number of points, the direct sum method is faster than the FMM because of the larger overhead in computational cost associated with the FMM. At very small N, the scaling is obscured by the computational overhead in both methods. Therefore, any deviation from scaling at small N should be ignored. At a few thousand points, the computational times for both methods are similar, and the $O(N^2)$ behavior is evident in the DSM data. For the FMM, the scaling becomes clear only when a very large number of mesh points is employed. For $N > 10000$, however, the overhead effects become negligible, and $O(N)$ behavior is clearly exhibited. The computational cost of the FMM is approximately given by $C_{FMM}N$, where the coefficient C_{FMM} is significantly greater than C_{DSM} and where $C_{DSM}N^2$ approximates the computational cost for the DSM. However, C_{FMM} is sufficiently

small enough that the FMM becomes much more efficient for the number of mesh points relevant for our simulation.

Our calculations typically have 4000 particles initially, each described by 128 to 256 points (for $L \approx 1$), resulting in $N = 512000$ to $1024000 \approx 10^6$. The elastic portion of the calculation takes approximately 40 CPU seconds each (first-level) time step for $N = 512000$. The direct sum method would have taken about two orders of magnitude longer, 4400 CPU seconds. Therefore, the simulations would not have been possible without using the FMM for the elastic field calculations.

9. CONCLUSIONS

A new set of numerical methods has been presented to accurately and efficiently simulate the evolution of microstructure in elastically stressed solids. These involved boundary integral methods, versions of the fast multipole method, and various time-stepping techniques. The result is a numerical method that can be employed to increase by orders of magnitude the number of particles simulated in a computational study of the evolution of microstructure.

In the process of developing the method, a number of issues were addressed:

1. A form for potentials in periodically arranged cells that is applicable in situations that require a general scheme to calculate a periodic potential via a summation in physical space.
2. An FMM for anisotropic linear elasticity that for large N is orders of magnitude faster than a direct sum method. The relevant dipole correction terms are introduced for unit cells that are parallelograms.
3. Introduction of a second-level time step for updating the shapes of particles. Although this approach should be used cautiously, it is possible to speed up the calculations by two additional orders of magnitude without a significant loss of accuracy.
4. A variable first-level time step as a function of the relative importance of the stress with respect to the interfacial effects.

Many of these techniques will have applications in other contexts as well.

The details are worked out specifically for our two-dimensional study. A corresponding simulation in three dimensions remains a challenge because of further complications such as the lack of analytic Green's function for the anisotropic elasticity problem [31]. However, the general ideas, such as incorporating the FMM, efficient time-stepping, and periodic potentials, can be extended for use in three-dimensional studies where similar issues need to be addressed.

ACKNOWLEDGMENT

KT is grateful for the hospitality of, and stimulating interaction with, W. C. Carter and his group at the Massachusetts Institute of Technology. We also thank National Science Foundation for its support through Grant DMR-9707073.

REFERENCES

1. N. Akaiwa and D. I. Meiron, Numerical simulation of two-dimensional late-stage coarsening for nucleation and growth, *Phys. Rev. E* **51**, 5408 (1995).

2. N. Akaiwa and D. I. Meiron, Two-dimensional late-stage coarsening for nucleation and growth at high-area fractions, *Phys. Rev. E* **54**, R13 (1996).
3. M. P. Allen and D. J. Tildesley, *Computer Simulation of Liquids* (Clarendon, Oxford, 1989).
4. A. J. Ardell and R. B. Nicholson, On the modulated structure of aged ni-al alloys, *Acta Metall.* **14**, 1295 (1966).
5. D. J. Bacon, D. M. Barnett, and R. O. Scattergood, Anisotropic continuum theory of lattice defects, *Prog. Mater. Sci.* **23**, 51 (1979).
6. C. L. Berman and L. Greengard, A renormalization method for the evaluation of lattice sums, *J. Math. Phys.* **35**, 6036 (1994).
7. D. Christiansen, J. W. Perram, and H. G. Petersen, On the fast multipole method for computing the energy of periodic assemblies of charged and dipolar particles, *J. Comput. Phys.* **107**, 403 (1993).
8. C. G. Lambert, T. A. Darden, and J. A. Board Jr., A multipole-based algorithm for efficient calculation of forces and potentials in macroscopic periodic assemblies of particles, *J. Comput. Phys.* **126**, 274 (1996).
9. P. Fratzl and O. Penrose, Ising-model for phase-separation in alloys with anisotropic elastic interaction 1. theory, *Acta Metall. Mater.* **43**, 2921 (1995).
10. A. Greenbaum, L. Greengard, and G. B. McFadden, Laplace's equation and the dirichlet-neumann map in multiply connected domains, *J. Comput. Phys.* **105**, 267 (1993).
11. L. Greengard and V. Rokhlin, A fast algorithm for particle summations, *J. Comput. Phys.* **73**, 325 (1987).
12. P. H. Leo and R. F. Sekerka, The effect of surface stress on crystal-melt and crystal-crystal equilibrium, *Acta. Metall.* **37**, 3119 (1989).
13. T. Y. Hou, J. S. Lowengrub, and M. J. Shelly, Removing the stiffness from interfacial flows with surface tension, *J. Comput. Phys.* **114**, 312 (1994).
14. H.-J. Jou, P. H. Leo, and J. S. Lowengrub, Microstructural evolution in inhomogeneous elastic media, *J. Comput. Phys.* **131**, 109 (1997).
15. K. N. Kudin and G. E. Scuseria, A fast multipole method for periodic systems with arbitorary unit cell geometries, *Chem. Phys. Lett.* **283**, 61 (1998).
16. J. K. Lee, Computer simulation of the effect of coherency strain on cluster growth kinetics, *Metall. Trans.* **22A**, 1197 (1991).
17. P. H. Leo, J. S. Lowengrub, and H.-J. Jou, A diffuse interface model for microstructural evolution in elastically stressed solids, *Acta Mater.* **46**, 2113 (1998).
18. P. H. Leo, J. S. Lowengrub, and Q. Nie, Microstructural evolution in orthotropic elastic media, *J. Comput. Phys.* **157**, 44 (2000).
19. I. M. Lifshitz and V. V. Slyozov, The kinetics of precipitation from supersaturated solid solutions, *J. Phys. Chem. Solids* **19**, 35 (1961).
20. J. A. Marqusee, Dynamics of late stage phase separations in 2 dimensions, *J. Chem. Phys.* **81**, 976 (1984).
21. J. A. Marqusee and J. Ross, Theory of ostwald ripening: Competitive growth and its dependence on volume fraction, *J. Chem. Phys.* **80**, 536 (1984).
22. G. B. McFadden, P. W. Voorhees, R. F. Boisvert, and D. I. Meiron, A boundary integral method for the simulation of two-dimensional particle coarsening, *J. Sci. Comput.* **1**, 117 (1986).
23. T. Mura, *Micromechanics of Defects in Solids* (Kluwer Academic, Dordrecht, 1987).
24. H. Nishimori and A. Onuki, Freezing of domain growth in cubic solids with elastic misfit, *J. Phys. Soc. Jpn.* **60**, 1208 (1991).
25. Y. Saad and M. H. Schultz, Gmres: A generalized minimum residual method for solving nonsymmetric linear systems, *SIAM J. Sci. Statist. Comput.* **7**, 856 (1986).
26. K. E. Schmidt and M. A. Lee, Multipole ewald sums for the fast multipole method, *J. Stat. Phys.* **89**, 411 (1997).
27. E. R. Smith, Electrostatic energy in ionic crystals, *Proc. R. Soc. Lond. A* **375**, 475 (1981).
28. C. H. Su and P. W. Voorhees, The dynamics of precipitate evolution in elastically stressed solids part ii: Particle alignment, *Acta Mater.* **44**, 2001 (1996).

29. T. Miyazaki, T. Koyama, and A. E. A. M. Mebed, Computer-simulations of phase-decomposition in real alloy systems based on the modified khachaturyan diffusion equation, *Metall. Mater. Trans. A* **26**, 2617 (1995).
30. M. E. Thompson, C. S. Su, and P. W. Voorhees, The equilibrium shape of a misfitting precipitate, *Acta Metall. Mater.* **42**, 2107 (1994).
31. M. E. Thompson and P. W. Voorhees, Equilibrium particle morphologies in elastically stressed coherent solids, *Acta Mater.* **47**, 983 (1999).
32. K. Thornton, N. Akaiwa, and P. W. Voorhees, A large-scale simulations of ostwald ripening in elastically stressed solids: I. development of micro structure, in preparation; K. Thornton, N. Akaiwa, and P. W. Voorhees, A large-scale simulations of ostwald ripening in elastically stressed solids: II. coarsening kinetics and particle size distribution, in preparation.
33. K. Thornton, N. Akaiwa, and P. W. Voorhees, The dynamics of late-stage phase separation in crystalline solids, *Phys. Rev. Lett.* **86**, 1259 (2001).
34. P. W. Voorhees, G. B. McFadden, R. F. Boisvert, and D. I. Meiron, Numerical simulation of morphological development during ostwald ripening, *Acta Metall*. **36**, 207 (1988).
35. P. W. Voorhees, G. B. McFadden, and W. C. Johnson, On the morphological development of second-phase particles in elastically stressed solids, *Acta Metall. Mater.* **40**, 2979 (1992).
36. C. Wagner, Theorie der alterung von niederschlägen der umlösen (ostwald-reifung), *Z. Elektrochem* **65**, 581 (1961).
37. Y. Wang, L. Q. Chen, and A. G. Khachaturyan, Kinetics of strain-induced morphological transformation in cubic alloys with a miscibility gap, *Acta Metall. et Mater.* **41**, 279 (1993).